M85010584

ORNL/TM--9471

DE85 010584

Fusion Energy Division

# THOMSON SCATTERING ON ELMO BUMPY TORUS

J. A. Cobble

Date Published - April 1985



Prepared by
OAK RIDGE NATIONAL LABORATORY
Oak Ridge, Tennessee 37831
operated by
MARTIN MARIETTA ENERGY SYSTEMS, INC.
for the
U.S. DEPARTMENT OF ENERGY
under Contract No. DE-AC05-84OR21400

# CONTENTS

# LIST OF TABLES

TABLE

# LIST OF FIGURES

FIGURE

# ACKNOWLEDGMENTS

The ELMO Bumpy Torus laser system has been a long-running show that has undergone development during three separate EBT managerial administrations. At one time or another, many people have been involved with improving, implementing, and assisting in the operation of this project. Key long-term supporters are R. E. Wintenberg, R. L. Livesey, M. W. McGuffin, and C. R. Schaich. Major contributions have been made along the way by M. Hesse, L. Bighel, T. L. White, P. W. King, L. A. Berry, and D. W. Swain. Ideas and equipment were shared generously by the Impurity Study Experiment Thomson scattering team.

# ABSTRACT

Below $10^{12}$ $cm^{-3}$ density, a Thomson scattering experiment is an exacting task. Aside from the low signal level, the core plasma in this instance is bathed in high-energy X rays, surrounded by a glowing molecular surface plasma, and heated steady state by microwaves. This means that the noise level from radiation is high and the environment is extremely harsh—so harsh that much effort is required to overcome system damage. In spite of this, the ELMO Bumpy Torus (EBT) system has proven itself capable of providing reliable $n_e$ and $T_e$ measurements at densities as low as $2 \times 10^{11}$ $cm^{-3}$. Radial scans across 20 cm of the plasma diameter have been obtained on a routine basis, and the resulting information has been a great help in understanding confinement in the EBT plasma. The bulk electron properties are revealed as flat profiles of $n_e$ and $T_e$, with density ranging from 0.5 to $2.0 \times 10^{12}$ $cm^{-3}$ and temperature decreasing from 100 to 20 eV as pressure in the discharge is increased at constant power. Evidence is presented for a suprathermal tail, which amounts to about 10% of the electron distribution at low pressures. The validity of this conclusion is supported by two independent sensitivity calibrations.

# 1. INTRODUCTION

For a decade, the ELMO Bumpy Torus (EBT) has been a central figure in the group of alternative concepts for the magnetic confinement of a fusion plasma.[1] Comprised of 24 mirror sections joined end to end to form a torus (Fig. 1), EBT has a major radius of 150 cm and an aspect ratio of 9.0. The plasma is driven by steady-state microwaves at the electron cyclotron resonance in the magnetic field. Initial experimental results with 30 kW of 18-GHz power (and half again that much at other frequencies) were encouraging,[2] and so began a series of machine and diagnostic upgrades with the aim of determining plasma scaling.

Thomson scattering has been among the key diagnostics on many plasma experiments for over 20 years,[3] and each experiment presents its own set of difficulties. For EBT the primary difficulty has been the low plasma density (2–8 $\times$ $10^{11}$ $cm^{-3}$). In spite of this, by 1976 McNeill and Dandl[4] had installed a 90° Thomson scattering system and had succeeded in obtaining laser data. Thirty or more laser shots were integrated at each of two wavelengths determined by a rotatable transmission filter. Those spectra, having a signal-to-noise ratio of about unity, were limited by plasma light. As the machine was upgraded, more obstacles were discovered in the search for an effective Thomson scattering diagnostic. The steady-state nature of the plasma presented an extremely harsh environment in which a delicate system of components was expected to survive. The story of the system evolution is as long as the history of EBT itself.[5] This report describes not necessarily the *best* but the *final* version of the Thomson scattering system on EBT.

ORNL PHOTO 8052-79


**Fig. 1. Photograph of EBT.** An early version of the Thomson scattering experiment is in the upper left.

In the next section, the laser and optical equipment is identified. Following that, the control and data acquisition circuitry is outlined (Sect. 3). From that point, the calibration and sensitivity of the system is discussed (Sect. 4), and Sect. 5 contains a sketch of the data analysis techniques. In Sect. 6 the capabilities of the system are illustrated with the results of several experiments in which the laser was used to measure the electron temperature $T_e$ and density $n_e$.

## 2. OPTICS

This section is a description of the optical equipment and the components used in the experiment. Figure 2 is a schematic of the apparatus, which consists of input beam optics, dumps, the collection optics, and the light-dispersion system.

The laser is a Q-switched ruby (Quantel model RB 58). An oscillator produces a 90-mJ, 25-ns pulse in the $TEM_{00}$ mode. This passes through four amplifiers, the last of which is 8 in. long and has a diameter of 1 in. The output is 25 J, with a maximum repetition rate of one pulse per minute. A half-wave plate is mounted on a rotation stage behind the oscillator. Backed by a cubic polarizer, this is used to reduce the beam energy in a controlled fashion without changing the temporal behavior of the pulse. This feature was useful for Rayleigh and Raman scattering runs. The ruby laser is relatively complicated to maintain and align. There are over 20 components, and the laser is unforgiving of errors. The punishment ranges from failure to oscillate to optical damage. A 25-mW, He-Ne laser has been a valuable alignment tool both within the laser box and downstream to the laser dump. The laser box is pressurized with $N_2$, which inhibits the migration of dust into the box and the formation of condensate on the cooled laser heads.

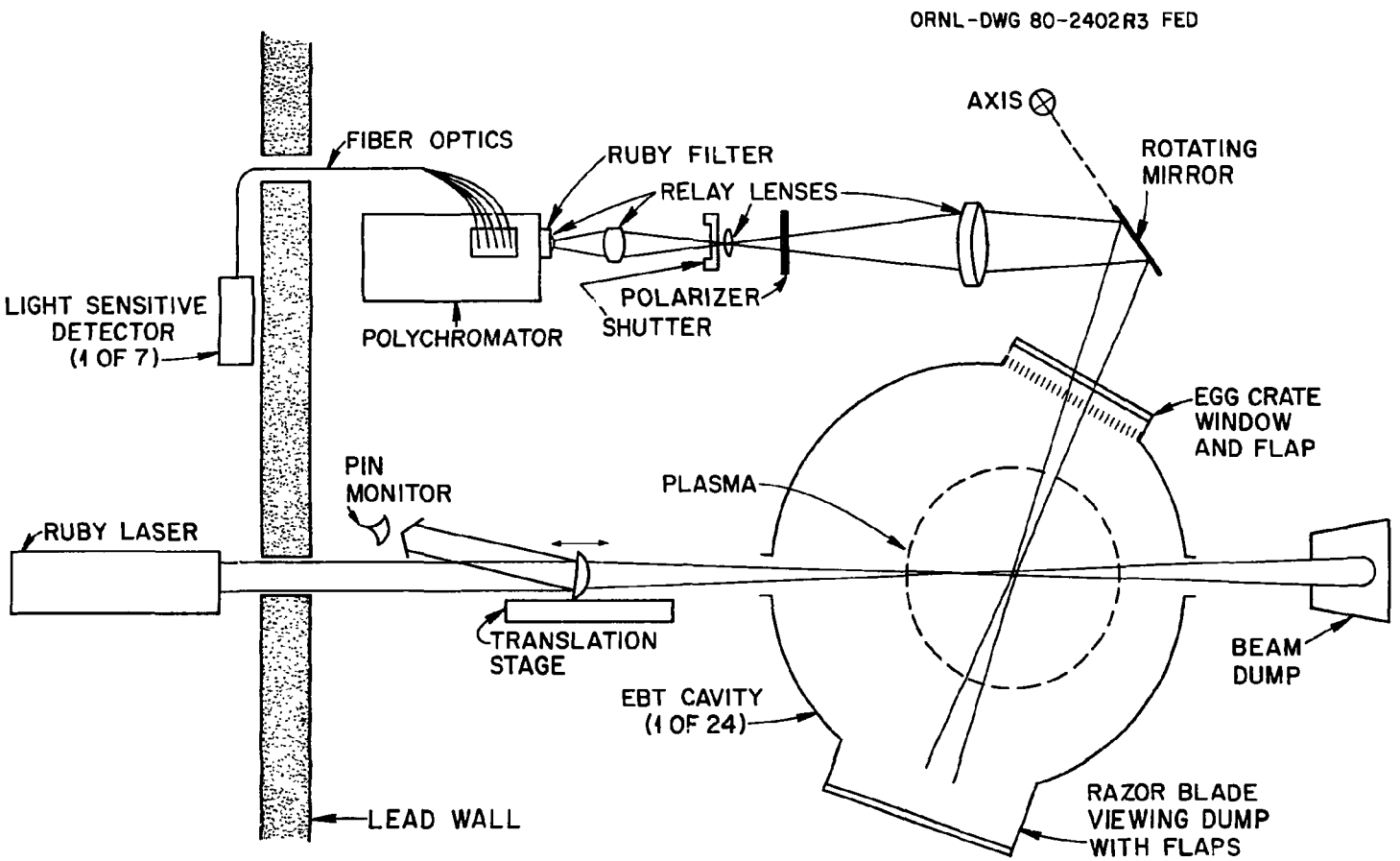


**Fig. 2. Schematic of Thomson scattering equipment on EBT.**

The beamline is a straight path to the lens that focuses the light in the plasma scattering volume, and a hole in the 6-in. lead radiation shield is required. A series of six baffles (circular apertures) is positioned just inside the lead wall to block stray light reflections originating in the tunnel through the wall, which is as small as possible. In fact, to control plasma radiation, a small lead shield blocks the tunnel. An air-operated piston swings the shield away prior to each laser shot and is part of a chain of permissive interlocks for firing the laser.

The focusing lens is plano-convex with a 2-in. diameter and has a focal length of 1 m. The material is suprasil, which enables it to survive the X-ray flux (1000–3000 R/h). After extended exposure, its red transmission still exceeds 90%, whereas in the violet this figure drops below 60% (Fig. 3). Antireflection coatings, incidentally, have not fared well between the 200-MW/cm$^2$ laser intensity and the high X-ray flux. The uncoated focusing lens is mounted on a remote control translation stage with a stepping motor and an optical encoder. Moving parallel to the optical axis, the lens can focus the beam anywhere along a 25-cm stretch through the plasma core. Unfortunately, the encoder was radiation damaged, but the lens position may be set by counting steps from the limit switch.

The vacuum interface is a suprasil window at Brewster's angle. Though the beam is converging, thus raising the power density, the angle doubles the area on the window through which the beam passes, and there has been no problem with damage. Because light is converging, Brewster's angle is only the average angle of incidence, and the small amount of laser light reflected is detected by a PIN diode, which serves as a trigger for data acquisition. A second PIN diode is used to monitor laser power reflected from the plane side of the focusing lens (Fig. 2), and considerable attenuation by filters is necessary

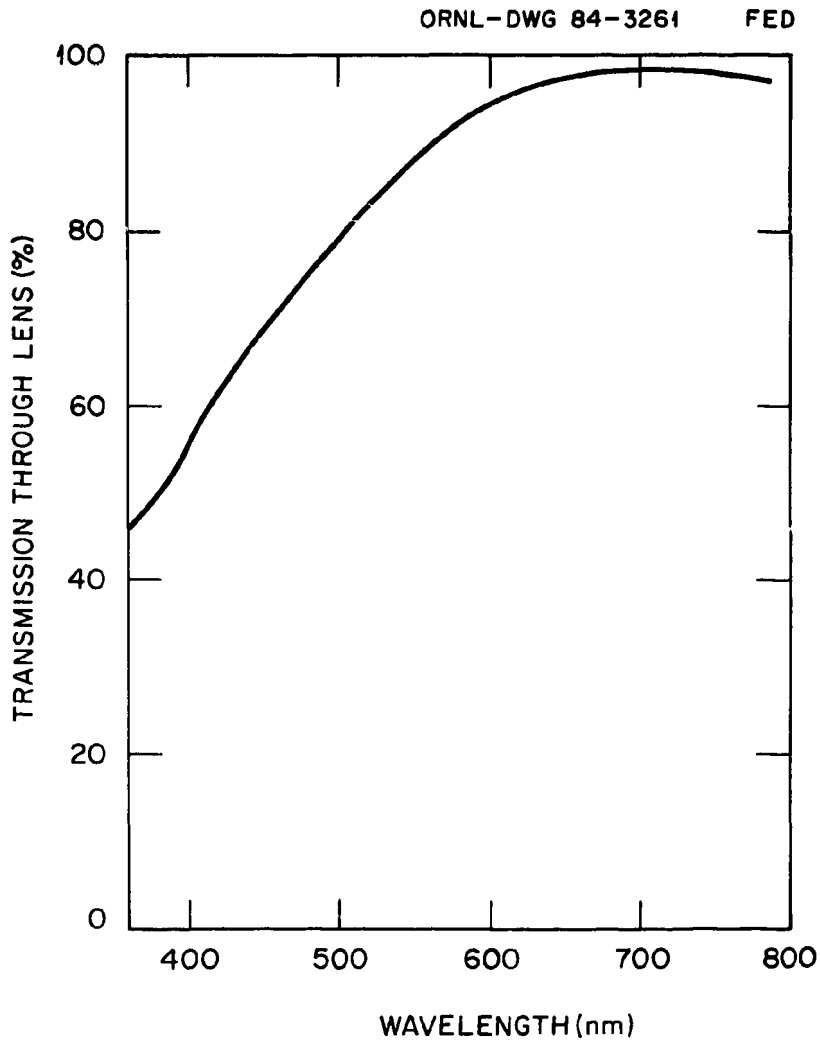


**Fig. 3. Transmission of suprasil exposed ($\approx 10^5$ *R* estimated) to hard X rays near EBT.**

because about a joule of energy is involved. The lens has to be tilted anyway to ensure that this reflected beam does not return to the laser amplifiers. To monitor the beam power accurately, it is important to prevent stray light from contributing to the PIN signal. One example occurs when the reflection from the curved face of the lens (again about a joule) causes air breakdown, and light from the spark bounces around the attenuation filters into

the PIN diode. Fortunately, the diodes have survived reasonably well in the high-radiation field.

A second permissive interlock for laser control is a limit switch on a flap that protects the Brewster window from sputtered aluminum from the plasma. As particles are deposited on the window, stray light progressively worsens. The flap is shaft mounted with a ferrofluidic feedthrough and is operated via a rotary solenoid. After passing the flap, the beam moves through a second series of six circular apertures that are needed not so much for stray light control as for attenuation of microwaves, which must not be allowed to escape from the machine. The baffles are coated with a microwave-absorbing material and are water cooled. The limiting aperture at the inner wall of the vacuum vessel has a diameter of 0.75 in.

The beam comes to a focus in a spot on the order of 500 $\mu$m across and then enters the beam dump as it expands. The dump itself is Schott glass BG7 at Brewster's angle. Because of the microwave power, it is face cooled with water. There are no baffles on the exit tube, but a flap has been installed to prevent aluminum sputtering on the dump. Before flap installation, damage was a problem, and stray light levels increased.

At the bottom of the plasma vessel is the viewing dump, which eliminates reflected plasma light and greatly reduces stray laser light. Its importance is realized when one considers that only about 100 of $8 \times 10^{19}$ photons per laser shot contribute to the Thomson scattering signal. If the others are not trapped in a black hole, the experiment is doomed. Because of the aluminum flux in the machine, a pair of flaps was installed over the viewing dump. The coating of the dump by aluminum was greatly retarded by this technique. In addition, the flaps catch the majority of metal flakes that fall toward the dump in the

bottom of the vacuum cavity. Such litter in the dump is a serious issue for other reasons since microwaves can cause it to glow incandescently. The dump flaps are another part of the permissive interlock system. The dump itself is fabricated with 32-cm-long, razor-edged blades stacked together and brazed to a water-cooled stainless steel plate. The blade edges are separated by 0.79 mm and have a minimum of fillet between them so that the dump appears as black as possible. Soaking the blade assembly in sodium hydroxide effectively removes any aluminum coating and leaves the surface very dark.

As the scattered signal leaves through a port on the top of the chamber, it passes through the so-called "egg crate." This is a thick, square-celled microwave cutoff screen. It is a 49 $\times$ 11 rectangular array of rectangular cells. The individual cell dimensions are 4.1 $\times$ 4.1 $mm^2$ by 6.0 mm deep with a 0.2-mm web thickness. Cold-test microwave transmission measurements at 28 GHz show a 27-dB attenuation. The normal incidence transmission of optical signals is 90%. The vacuum window is a 20 $\times$ 5 $cm^2$ piece of suprasil. Between it and the egg crate is a flap (Fig. 4) to protect the window from sputtered aluminum. The interlocked flap is open for a laser shot (about a fourth of a second for each); the aluminum flux is greatly reduced by the egg crate. Much of the aluminum has an angle of incidence $\phi$ on the egg crate that is significantly different from zero so that there is no straight path through.

Once outside the vacuum vessel, the signal is reflected by a dielectric mirror into a system of collection lenses. The mirror can be rotated to focus light on the polychromator slit from different regions of the plasma. The distance $S_1$ from the large collection lens to the scattering volume is maintained constant within 1% by rotating the mirror about an

ORNL PHOTO 7432-84

**Fig. 4. Photograph of the egg-crate window with the flap opened on the right side.**

axis 20 cm above the lens axis (Fig. 5). A 15° rotation enables a 20-cm shift in the position of the scattering volume in the plasma. (This must be done in conjunction with the translation of the focusing lens to ensure maximum laser intensity in the scattering volume.) The shift in the image position along the optical axis at the polychromator slit due to changes in $S_1$ is about 1 mm. This defocusing effect is no larger than the random error in alignment of the entire system and may be reduced to some extent by opening up the polychromator slit. An additional loss of signal at the extremes of a radial scan comes from the increase of $\phi$ from 0° to about 7°. Table 1 shows the relative sensitivity of the system for different radial positions. (The variation of the scattering angle $\theta$ is shown, too.) Because of the increase in $\phi$, the defocusing, and the random misalignment, the sensitivity at the ends of the scan is only about half of the maximum value.

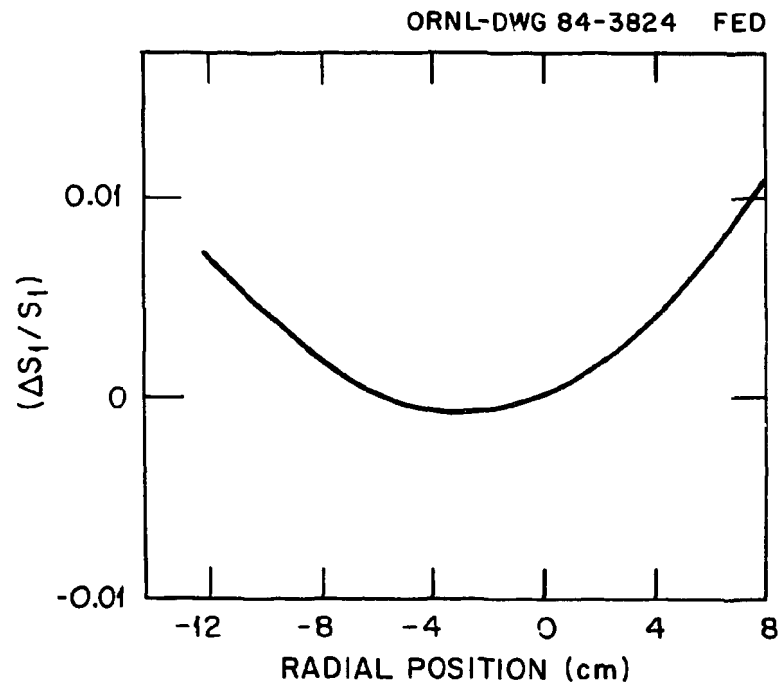


**Fig. 5. The fractional change of the object distance $S_1$ during a radial scan of the scattering volume by the rotating mirror.**

**Table 1. The sensitivity, scattering angle, and stray light for different radial positions**

| Radial position (cm) | Sensitivity, $N_R$ (bits per torr) | Scattering angle, $\theta$ (degrees) | Stray light, $S_0/M$ (torr) |
|---|---|---|---|
| −12 | 39 | 81 | 14 |
| −8 | 51 | 78 | 7.6 |
| −4 | 86 | 75 | 1.5 |
| 0 | 89 | 72 | 0.5 |
| +4 | 80 | 69 | 0.7 |
| +8 | 47 | 66 | 1.7 |

The collection lenses (Fig. 6) are selected to couple light into the polychromator in such a way that (1) the collection solid angle $\Omega$ is a maximum, (2) the grating is filled, and (3) the sizes of the lenses are minimized. The large collection lens $L_1$ focuses the beam onto a slit at an intermediate focal plane at the field lens $L_2$. This is very useful for controlling stray laser light. $L_2$ has a minimal effect on the signal focus because it is virtually in the focal plane. A third lens, $L_3$, relays the signal onto the polychromator slit through a final field lens $L_4$. The purpose of the field lenses ($L_2$ and $L_4$) is to reduce the required diameters of $L_1$ and $L_3$. The focal length of $L_4$ is chosen to focus the grating on $L_3$. Similarly, the focal length of $L_2$ has been chosen to form a second image of the grating at the collection lens ($L_1$). $L_1$ and $L_3$ are two-element lenses specially designed to avoid spherical aberrations. $L_2$ and $L_4$ are simple lenses. All are made of suprasil and are anti-reflection coated. Table 2 lists the diameters and focal lengths and the approximate separation distances indicated in Fig. 6. Since $L_2$ and $L_4$ are thick lenses and the distances cannot be measured with precision, the beam magnification $M_b$ and the grating magnification $M_g$ may only be approximated. Another proviso is that in the original spectrometer, the focal length $G$ was 25 cm. When the spectrometer was later modified, $L_4$ was not changed. The required change in focal length was scarcely more than the expected error in

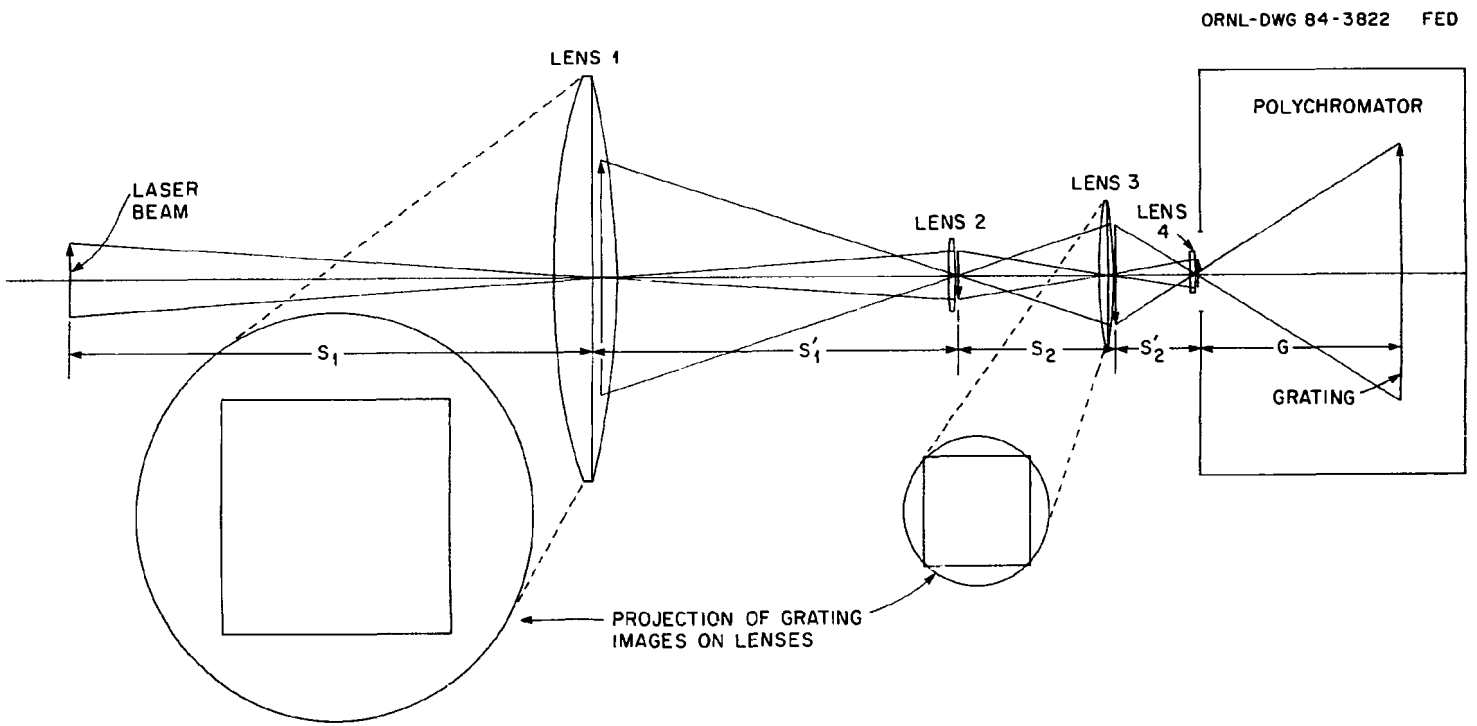


**Fig. 6. A schematic ray trace of the collection optics for estimating the solid angle.** Lens properties are given in Table 2.

**Table 2. Lens characteristics[a]**

| Lens | Diameter (cm) | Focal length (cm) |
|---|---|---|
| $L_1$ | 14 | 30 |
| $L_2$ | 5 | 15 |
| $L_3$ | 5 | 7.6 |
| $L_4$ | 2.1 | 8.0 |
| Approximate spacings, cm | | |
| $S_1$ | 75 | |
| $S_1'$ | 50 | |
| $S_2$ | 21.3 | |
| $S_2'$ | 11.8 | |
| $G$ | 28.9 | |

[a]Illustrated in Fig. 6.

manufacture. The result is that the grating images do not fall exactly on $L_1$ and $L_3$. Nevertheless, the estimated values of magnification are $M_b \sim 0.37$ and $M_g \sim 0.85$. Knowing the grating dimension $h$ ($h \sim 9.5$ cm), a fair estimate of the collection solid angle is

$$\Omega \sim (hM_g/S_1)^2 = 0.012 \text{ steradians} . \quad (1)$$

In principle, minor changes in the focal lengths of the field lenses could enable better use of $L_1$, thereby increasing $\Omega$ by about 25%. However, uncertainties in $M_g$ suggest the result might be more modest.

Additional equipment in the collection beamline (Fig. 2) includes a mechanical shutter, a polarizer, and a ruby absorption filter. The Uniblitz shutter is located at $L_2$ and has a 1-in. aperture. It serves to keep plasma light away from the photocathodes of the detectors even when the flaps are open. The dc level of plasma light draws very close to the maximum recommended average anode current in the phototubes. Even though the

gain may be turned off, as discussed later, a decision was made not to expose the photocathodes for quarter-second intervals. The shutter, which is the last of the interlocks to ... up, fires the laser. The total open time is 7 ms. The next item, a polarizing filter, gives a very high level of rejection of one polarization while transmitting about 70% of the other. Since the Thomson scattering signal is polarized, the filter improves the signal-to-noise ratio by cutting the randomly polarized plasma light in half. Finally, the ruby filter,[6] located adjacent to the polychromator slit and $L_4$, is a small, 7.4-mm-thick disk of synthetic ruby. Doped with 1% chromium and antireflection coated, it reduces stray laser light by nearly two orders of magnitude. Figure 7 shows the transmission of polarized light by a properly oriented ruby filter. The absorption depends on the angle of the polarization with respect to one of the crystal axes. The transmission characteristics, incidentally, encourage

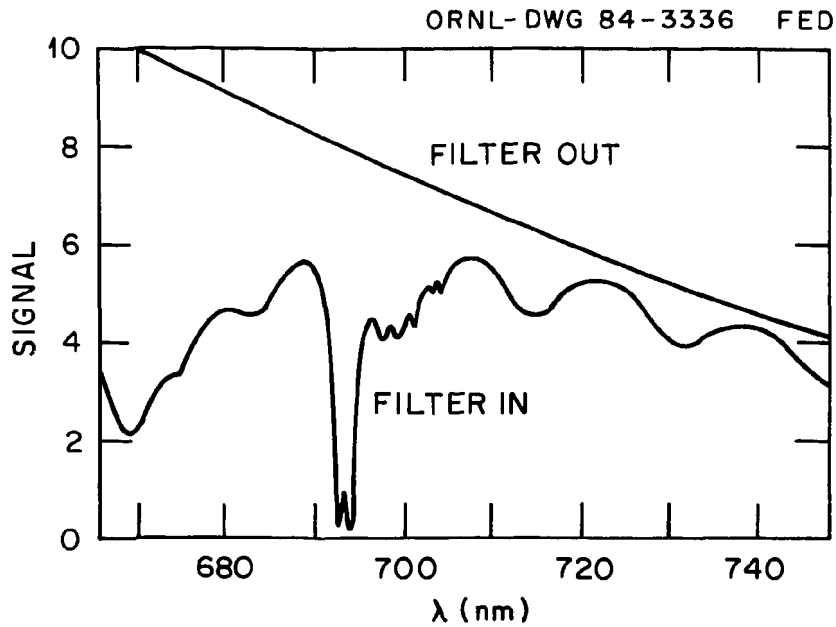


**Fig. 7. Transmission of polarized light through an antireflection-coated ruby filter: the upper line is the spectrometer signal without the filter; the lower line is with the filter.**

taking data on the long-wavelength side of the 694-nm laser line where the transmission is higher and more uniform.

The light-dispersion system consists of a polychromator with fiber optic bundles in the exit focal plane to transmit the signal to phototubes. The polychromator (a Minuteman Model 302 TS) has a large, concave, holographic grating (9.5 × 9.5 $cm^2$). The entrance slit width is adjustable. It is typically set at 500 $\mu$m, a factor of about 2 larger than necessary (for reasons already mentioned). The slit height is 10 mm. Light is incident on the grating at 9.5°. The zeroth order is dumped into a light trap. The first-order light is focused into a staggered array of fiber optic cables. These cables are 2.1 m long and run through the radiation shield in a conduit. Made of suprasil, the measured transmission is nearly 60%. There has been no degradation by X rays. Table 3 shows the individual properties of the bundles, that is, cross section, wavelength range, and central wavelength.

**Table 3. Fiber optic channels in the polychromator**

| Channel | Cross section ($mm^2$) | Range[a] (nm) | Mean λ (nm) | Reduced wavelength, ϵ |
|---|---|---|---|---|
| 1 | 11 × 1.5 | 698.8–703.8 | 701.3 | 0.010 |
| 2 | 11 × 1.5 | 706.6–710.8 | 708.7 | 0.021 |
| 3 | 11 × 3 | 710.8–719.1 | 715.0 | 0.030 |
| 4 | 11 × 3 | 720.0–727.1 | 723.6 | 0.042 |
| 5 | 11 × 3 | 729.2–737.0 | 733.1 | 0.056 |
| 6 | 11 × 3 | 737.9–745.5 | 741.7 | 0.068 |

[a]Full width at half maximum (FWHM).

The phototubes (Hamamatsu R943-03) have gallium arsenide photocathodes with quantum efficiencies of 10 to 14%. However, the photocathodes are small (1 $cm^2$) and are recessed 2 cm inside the tube end. To couple the light from the fiber optic bundles to the photocathodes, f/1.2 camera lenses were used. Fortunately, the f number of the signal out

of the bundles is nearly the same as the f number of the signal going in. Care is taken to align the bundles so that their axes point toward the center of the grating. A light-tight box holds mounts for the bundle ends, the camera lenses, and the tubes. By pointing a bundle at a bright point source, a mirror can be used to adjust a tube in its socket. The circular image of the output end of the fiber bundle is projected with unity magnification onto the photocathode. Black paper is used to prevent crosstalk between channels.

## 3. ELECTRONICS

A rather intricate electronic circuit is required to coordinate an active plasma diagnostic such as Thomson scattering. Timing is the key word, both in the long time limit during which the laser repetition rate must not be exceeded and in the short time limit during which many subsystems must be coordinated to record the 50-ns–duration signal. Figure 8 is a block diagram of the main features of the logic. For ordinary operation, the EBT computer directs data acquisition. (Oscillograms are periodically taken to check timing.) The preliminary activity requires setting the radial position—the input lens and the mirror positions. The control program then accepts information on the position, the number of laser shots in the sequence, and the run type (whether Thomson, Rayleigh, Raman, stray light, etc.). A discussion follows on two aspects of the electronics—laser fire control and gate generation.

The energy storage capacitor banks for the laser may be charged manually or automatically. The firing order may be initiated manually or automatically, too. Generally these tasks are done automatically by the computer. The fire control is provided by a

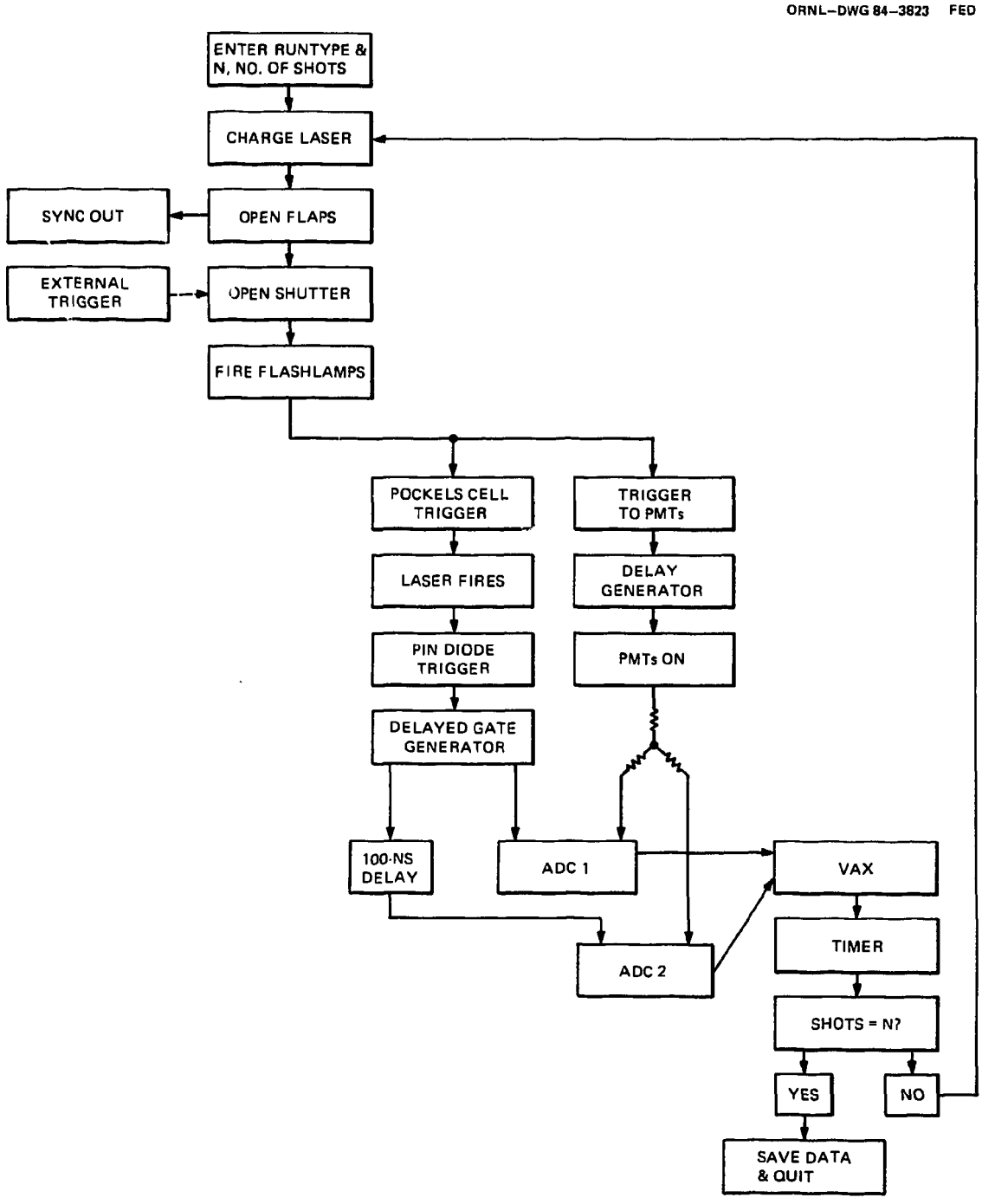


**Fig. 8. Block diagram of the electronic logic circuit for controlling the Thomson scattering experiment.**

custom-built panel that performs a number of operations. Once the fire signal arrives, the interlocked flaps begin to open. There are five of these, including the lead plug at the radiation wall. When the interlocked limit switches of these permit it, a signal is sent to the shutter.* The shutter opens in a predictable time, after which the flashlamps are fired. The same signal that triggers the flashlamps initiates two delayed triggers: one serves as a phototube switch; the other, which occurs 25 $\mu$s later, fires the Pockels cell and the laser.

Several critical timing events must be synchronized now. One involves turning on the phototubes. Recall that for each laser shot, the photocathodes are exposed to intense plasma light for 7 ms. To limit the active time of the tubes, the first and third dynodes are reverse biased. At the appropriate time, a 25-$\mu$s gate forward biases the dynodes. The dc level changes for the first 20 $\mu$s before coming to equilibrium. Thus, the scattered photons are scheduled to reach the tubes about 20 $\mu$s after they turn on.† The phototubes are dc-coupled to LeCroy VV100 preamps. Care must be taken to maintain a negative dc level at less than 5 mV. The 100-ft transmission lines between the detectors and the signal processors are terminated with balun coils for removing low-frequency ripple. The signal lines are divided, impedance matched, and fed into gated integrators (LeCroy 2249As) that perform analog-to-digital conversion. The gates for the integrators are generated by the passage of the beam into the plasma chamber. Signal from the Brewster window PIN diode triggers a delayed gate generator. There are several parallel output gates. The delay is set so that the

---

*The shutter trigger source may be supplied externally; for time-dependent measurements (e.g., gas puffing or microwave pulsing), external mode is used.

†Gallium arsenide tubes do not have a history of good behavior. The dynode switching was an attempt to prolong the useful lifetime of the tubes. Once this activity began, Thomson scattering signal levels from equivalent plasmas did not change appreciably over a period of several months. A slight downward trend was consistent with the manufacturer's shelf-life measurements, but the reduction could have been due to differences elsewhere in the system.

arrival of the scattered signal is simultaneous with the arrival of the gate at the second integrator, ADC 2 (Fig. 8). The integration time is set at about 65 ns to allow a little extra time to accommodate drifts, cable time, and the base of the laser's temporal profile. The first integrator records plasma light 100 ns before the pulse. In practice, the large laser signal in the first data channel often showed overshoot. This could cause a systematic underestimation of plasma light in the channel if the noise were measured after, rather than before, the signal.

After each laser shot, the data are shipped to the computer, which displays and stores shot number, time, signal, and pedestal level (the integrator output with no input) for each channel for both integrators. A timer cycles to prevent the laser from being fired too rapidly and then, if the requisite number of shots is not yet reached, begins charging the laser. Otherwise, the experimenter can cause the data file to be stored or take more data.

## 4. CALIBRATION AND SENSITIVITY

Making the Thomson scattering measurement requires several calibrations—the wavelength calibration of the polychromator, the relative sensitivities of the detectors, and the density calibration. The first of these is a measurement seldom done. The second is important because of the suspicion with which gallium arsenide tubes have come to be regarded. Finally, the density calibration must be done more frequently, every 2 to 4 weeks, because this is a good monitor of overall system performance; it provides a good bench mark of whether and how much something has changed.

The wavelength calibration is the means by which the polychromator is adjusted to set the wavelength channels. In setting up the optics for detection, the polychromator is the first component on the optics rail. The fiber bundles are joined to it, and the wavelength calibration is next. A 0.25-m monochromator is used to filter an incandescent lamp and to transmit a 0.8-nm band of light into the entrance slit of the polychromator. As the calibrated, servo-controlled grating in the monochromator is turned, signal from a detector mounted onto a fiber bundle is observed on an $x$-$y$ recorder. The detector response as a function of wavelength is reasonably well characterized as flat on top with rapidly falling sides. The half-intensity points are taken as the channel boundary from which a mean wavelength is calculated for the channel. All channels are measured in this way after the polychromator grating is adjusted to the desired position. In this case, the desired orientation is such that an aluminum multiplet centered at 704.9 nm falls between the first two data channels. Once set, it is unnecessary to repeat this measurement until the fibers are disconnected from the polychromator.

A hint for system alignment may be inserted at this point. After adjusting the input lens, a moveable target probe inclined at 45° may be placed at the focal point and a low-power laser burn made on the black target. The He-Ne laser mentioned earlier may be checked to see if it illuminates the burned region of the target. The light reflected from the target may then be used to position all components of the collection optics.

The second calibration task, determining the relative sensitivities of the data channels, is accomplished by placing a calibrated lamp behind a diffuser plate between the egg-crate window and the dielectric mirror. Several thousand gates are generated to trigger the phototubes and the integrators. Using neutral density filters, the lamp intensity is adjusted

so that no signal is present during most gates. Therefore, when a signal is present, it is most likely due to a single photoelectron. The gate width is long compared to the transit time of a photon signal. The number of nonzero responses is proportional to the quantum efficiency of a channel. The average amplitude of the nonzero responses is proportional to the channel gain per photoelectron. The relative sensitivity is just the product of these two factors. Values so obtained are judged to be correct within 10%. Tube gain, incidentally, is controlled from a panel with individual potentiometers for each tube and a digital voltmeter to monitor tube voltage. It is important to check the relative responses of ADC 1 and ADC 2 to identical signals for each channel. If the gates are slightly different or if the bits per picocoulomb are not the same, trouble occurs in the high-energy channels where the Thomson scattering signals vanish. As nature would have it, the plasma molecular radiation is several times worse in the outer channels. In fact, the inequality of plasma light in parallel integrators here where no laser signal is expected is a sign that the integrators are not equivalent and need to be calibrated.

Final system alignment is done by Rayleigh scattering on about 10 torr of $N_2$. Laser energy is reduced to 5–8 J via the half-wave plate after the oscillator to prevent ionization of the gas, and the ruby absorption filter is set aside. Signal is detected in a separate fiber optic channel at 694 nm. Micrometer screw adjustments on the positions of the slit at $L_2$ and the polychromator slit are made to optimize the Rayleigh signal. The signal $S$ depends linearly on the pressure $p_0$ and should nearly vanish as the gas is pumped out of the plasma vessel:

$$S = Mp_0 + S_0 \ . \tag{2}$$

The stray light, the figure of merit, $S_0/M$ is given in Table 1 for the various radial positions. Why the stray light increases at $-8$ and $-12$ cm is not understood.

The density calibration is done with Raman scattering on $H_2$. The ruby filter is replaced, and channels used for Thomson scattering are employed to gather the Raman spectra. (Use of the ruby filter precludes use of the Rayleigh channel for Thomson scattering data.) The strongest Raman line is at 723.8 nm. The Raman scattered signal per torr $N_R$ is given by

$$N_R = N_L(R) n_H (\sigma_R/\sigma_T) r_0^2 \ell \Omega \eta S_R \ , \tag{3}$$

where $N_L(R)$ is the number of laser photons through the scattering volume, $n_H$ is the density of hydrogen at 1 torr during Raman scattering, $\sigma_R/\sigma_T$ is the ratio of cross sections of Raman scattering on $H_2$ to Thomson scattering,[7] $r_0$ is the classical electron radius, $\ell$ is the length of the scattering volume, $\eta$ is the system transmission, and $S_R$ is the sensitivity of the Raman channel normalized to the first data channel. A similar expression gives the Thomson scattering signal $N_T$:

$$N_T = N_L(T) n_e r_0^2 \ell \Omega \eta F S_T \ . \tag{4}$$

Note that $N_L(T)$ is 3 to 5 times bigger than $N_L(R)$ because of the half-wave plate. This factor is defined as

$$P = \frac{N_L(T)}{N_L(R)} \ . \tag{5}$$

$S_T$ is the sensitivity of the Thomson channel. Because the Thomson scattering spectrum may be spread across many data channels, another term is needed. $F$ is the fraction of the Thomson spectrum that would fall in a channel at the laser wavelength. It is found by integrating a normalized Maxwellian distribution from the laser wavelength to the edge of the central channel. For this experiment,

$$F = \text{erf}\left[\frac{0.8}{\sin\frac{\theta}{2}\sqrt{T_e}}\right], \tag{6}$$

and $N_T$ [Eq. (4)] is then the amplitude of scattered spectrum at the laser wavelength. Combining Eqs. (3) and (4), substituting constants, and solving for $n_e$, one gets

$$n_e = \frac{7.76 \times 10^{10} N_T S_R}{N_R P F S_T} . \tag{7}$$

Note that before $n_e$ can be determined, a spectrum analysis must be completed to find $N_T$, $T_e$, and thus $F$. In practice the density calibration must be repeated frequently. Alignment is extremely critical, and a bump is a cause of concern—in the imagination, if not in fact. Another common worry is that the transmission has degraded since the last calibration. A window coating due to a flap malfunction, for example, means that $\eta$ no longer cancels out of Eq. (7). Other past difficulties have included changes in the laser energy and drift in the timing so that some part of the signal misses the integration gate.

The pressure dependence of Raman scattering is shown in Fig. 9. The slope of the line gives $N_R$. A second benefit of Raman scattering is that it makes possible an independent

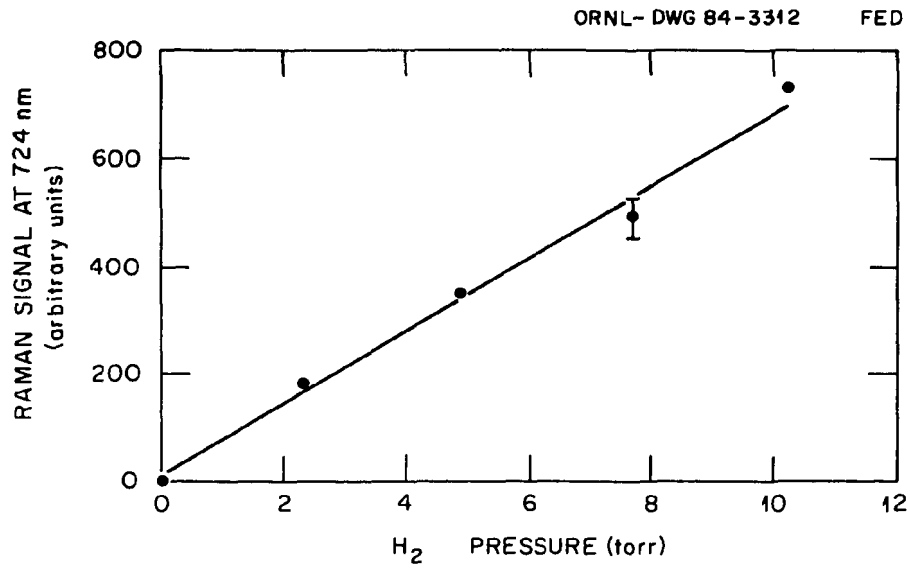


**Fig. 9. The pressure dependence of Raman scattering on $H_2$.** The points represent the average values of three laser shots at each pressure.

channel sensitivity calibration. By coincidence, the Raman lines at 711.8 and 723.8 nm fall unambiguously in different data channels. The ratio of $N_R$ values equals the ratio of the Raman cross sections, which are given to 10% accuracy. This measurement imparts confidence to the diffuser plate calibration of phototube sensitivities.

It is instructive to use Eq. (4) to calculate the expected number of photoelectrons in a laser shot. Assume scattering were done on a 50-eV plasma with a density of $8 \times 10^{11}$ cm$^{-3}$. Table 4 lists the values of parameters in the equation. $N_L$ assumes a 25-J laser shot with losses only at an uncoated focusing lens. The reciprocal of $M_b$ is used for $\ell$, the length of the slit image along the laser beam. The transmission factor includes all components between the plasma and the tube photocathodes, which are assumed to be 10% efficient. With $\theta = 72°$, $F$ is determined from Eq. (6). Finally, the product of these terms must be divided by 2 because the signal is split between two integrators. The resulting 80

**Table 4. Photon inventory for EBT laser system[a]**

| | | |
|---|---|---|
| $N_L$ | | $8 \times 10^{19}$ |
| $n_e$, $cm^{-3}$ | | $8 \times 10^{11}$ |
| $r_0^2$, $cm^2$ | | $7.9 \times 10^{-26}$ |
| $\ell$, cm | | 2.7 |
| $\Omega$ | | 0.012 |
| $\eta$ | | |
| Uncoated glass | $(0.92)^2$ | |
| Coated glass | $(0.98)^4$ | |
| Mirror | (0.98) | |
| Egg crate | 0.9 | |
| Polaroid | 0.7 | |
| Ruby filter | 0.7 | |
| Polychromator | 0.25 | |
| Fiber optics | 0.55 | |
| | 0.046 | 0.046 |
| $F$ | | 0.215 |
| $QE$ | | 0.1 |
| $N_T$ (calculated) | | 81 |
| $N_T$ (measured) | | 27 |

[a]See Eq. (4).

photons represent the largest number of counts for the assumed plasma with perfect alignment and perfect coupling to the photocathodes. This is not the number of photons in the whole spectrum but in a 4.4-nm band at the center (the basis for the sensitivity normalization). In practice, about one-third of this number is actually counted. The reason for the discrepancy is unknown, though candidates are numerous (e.g., overestimates of quantum efficiency, grating efficiency, beam quality, and alignment).

Data are typically collected in a 10-shot sample. As an example of the capabilities of the EBT laser system, consider the correlatio of the central value of $n_e$ versus the line-integrated density $n_e\ell$ obtained with a 70-GHz interferometer (Fig. 10). At the highest machine pressure, the plasma seemingly fills the entire 50-cm diameter of the vessel. As pressure is lowered, confinement improves and the plasma takes on the diameter allowed by a limiter used in this experiment. At lowest pressures, the density profile is quite likely peaked in the center, which accounts for the departure of the curve from the origin.

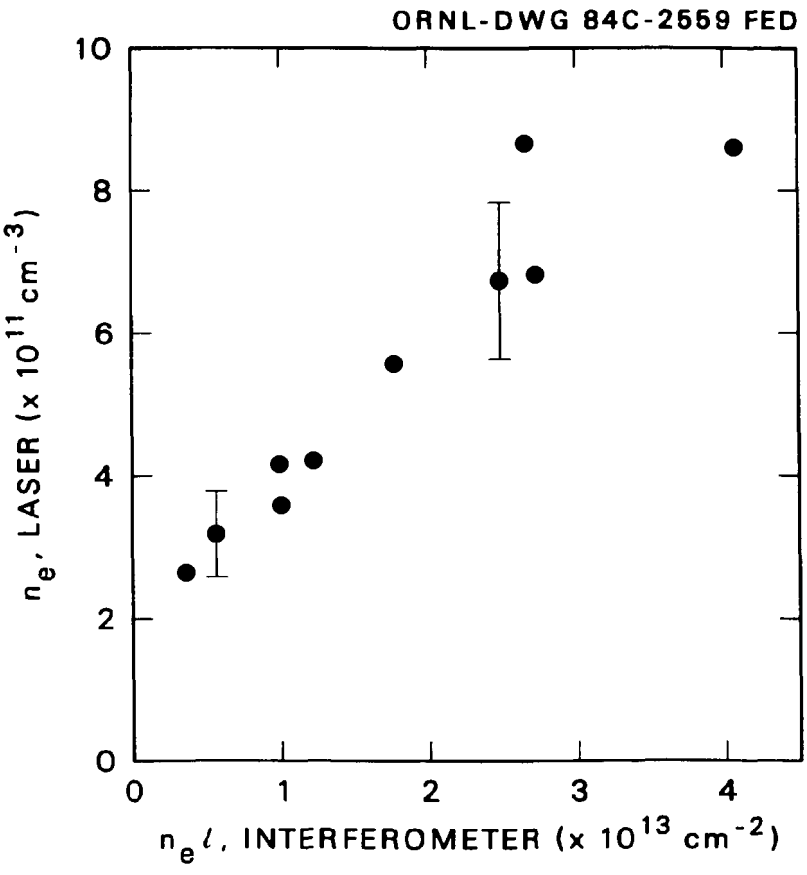


**Fig. 10. The correlation of central electron density measured by Thomson scattering and line-integrated density from a microwave interferometer.**

Regrettably, no profile data were obtained for these cases. (It is an inherent disadvantage that a 10-shot sequence takes 10 min; a six-point radial scan takes an hour; and radial scans for $N$ conditions take $N$ hours). In any case, the system has shown the ability to measure a density of $2 \times 10^{11}$ $cm^{-3}$. Because the number of counted photons in that 10-shot sequence exceeded 100, the real lower limit (depending on the patience of the experimenter) may be even less.

# 5. DATA ANALYSIS

This section contains a discussion about the way in which Thomson scattering data were gathered and analyzed on the steady-state EBT plasma. As already noted, the experiment was largely computer controlled. The laser was fired by the computer a set number of times; the data were acquired and saved. Afterwards, the data could be examined by further interaction with the EBT computer.

Typically, ten laser shots taken at the same position with the same plasma conditions comprised a data sequence. Each sequence was matched with an accompanying plasma light sequence since the signal was split between two integrators. Integrator pedestals were monitored a second after each laser shot and then subtracted. The key values generated from each sequence were the mean $\mu$ and variance $\sigma^2$ of each of the six wavelength channels and the laser power monitor. The scattered signals were normalized on each shot for laser power. If the laser misfired or if its power dropped by a certain fraction, the sequence would be interrupted. In order to do an analysis, values of $\mu$ and $\sigma^2$ were required for the Thomson signals, TS, the plasma light signals, PL, and a stray light sequence, SL, taken at the same radial position. The final processed values for the analysis routine are

$$\mu_I = \mu_{TS} - \mu_{PL} - \mu_{SL} \tag{8}$$

and

$$\sigma_I^2 = \sigma_{TS}^2 + \sigma_{PL}^2 + \sigma_{SL}^2 \ , \tag{9}$$

where $i$ is the channel number. The values labeled TS include contributions from both plasma light and stray laser light and are thus corrected.

For a given sequence, the Thomson scattering spectrum is $\mu_i$ as a function of $\epsilon_i$ (the reduced wavelength of the $i$th channel). This last term is defined as the difference between the channel mean wavelength and 694.3 nm divided by the latter (see Table 3). Electron distributions are historically taken to be Maxwellian so that a plot of ln $\mu$ versus $\epsilon^2$ is expected to be a straight line, the slope of which is inversely proportional to $T_e$. Owing to the luxury of computer analysis, a first-order relativistic correction was made. Ordinarily, this does not become important until $T_e$ is greater than 100 eV. The Maxwellian model for the photon number $y$ becomes

$$y = \mu(\epsilon, N_T, B) = N_T(1 - 2.5\epsilon)\exp B\epsilon^2/(1 + \epsilon) \ , \tag{10}$$

where

$$B = -mc^2/8T_e \sin^2\theta/2 \ , \tag{11}$$

and $mc^2$ is the electron rest mass energy. $N_T$ is in the limit of low $T_e$ identical with that appearing in Eq. (7). [If $T_e$ becomes large, the definition of $F$ from Eq. (6) must be modified.]

Following is a description of the data-fitting routine—a weighted least-squares fit using Eq. (10). The routine works equally well for any model. Details may be found elsewhere.[8] The observed values of the dependent variable (signal amplitude) are

$$Y_i = \mu_i \ . \tag{12}$$

The variance of $Y_i$ is of course $\sigma_i^2$. It is assumed that the independent variable $\epsilon_i$ is known and has negligible variance. The object of the fitting routine is to determine the unknown parameters in the model, $a_1$ and $a_2$, where

$$y(\epsilon, a_1, a_2) = \mu(\epsilon, N_T, B) \ . \tag{13}$$

Having successfully fit for $a_1$ and $a_2$, that is, $N_T$ and $B$, Eqs. (7) and (11) may be used to derive $T_e$ and $n_e$. A function $F_i^0$ is defined as

$$F_i^0 = Y_i - y_i(\epsilon_i, a_1^0, a_2^0) \ , \tag{14}$$

where the superscript implies an initial guess. A perfect fit of the data to the model would leave $F_i^0$ everywhere equal to zero. The figure of merit is the sum of the least squares or, as it is called in this case, the weighted sum of the squares of the residuals:

$$S = \sum_{i=1}^{n} \frac{F_i^2}{\sigma_i^2} \ . \tag{15}$$

This is a minimum for the best fit, and in an experimental situation, were the measurement made many times, $S$ should be distributed as a chi-square function, the mean value of which is

$$\langle \nu \rangle = n - p \ . \tag{16}$$

The number of data points (wavelength channels) is $n$, and $p$ is the number of unknown parameters (equal to 2 in this case). The difference $\nu$ is the number of degrees of freedom.

To minimize $S$, a matrix equation must be solved:

$$A_k = \sum_{j=1}^{p} C_{kj}^{-1} \mathbf{V}_j = a_k^0 - a_k \ , \tag{17}$$

where $k = 1,...p$ and where $a_k$ is the new value for the $k$th unknown parameter. The best-fit value of $a_k$ is reached as $A_k$ approaches zero in successive iterations. The elements of the vector **V** are given by

$$\mathbf{V}_j = \sum_{i=1}^{n} F_i^0 \frac{\partial F_i^0}{\partial a_j} \Big/ \sigma_i^2 \ . \tag{18}$$

The matrix **C** has elements given by

$$C_{jk} = \sum_{i=1}^{n} \frac{\partial F_i^0}{\partial a_j} \frac{\partial F_i^0}{\partial a_k} \Big/ \sigma_i^2 \ . \tag{19}$$

Its inverse is calculated by standard techniques.

After the iterative routine has converged, the best values of the unknown parameters are known, and their variance is determined via

$$\sigma_{a_k}^2 = S \ \frac{C_{kk}^{-1}}{(n-p)} \ . \tag{20}$$

From these, an operational error bar for $T_e$ and $n_e$ may be calculated, namely, the standard deviation. For $T_e$,

$$\Delta T_e = \sigma_{T_e} = T_e \frac{\sigma_{a_2}}{a_2} \quad , \tag{21}$$

where $a_2$ is $B$ [Eq. (11)]. Also,

$$\Delta n_e = n_e \left( \frac{\sigma_{a_1}^2}{a_1^2} + \frac{\sigma_F^2}{F^2} \right)^{1/2} \quad . \tag{22}$$

The variance of $F$ may be calculated via

$$\sigma_F^2 = \sigma_{a_2}^2 \left( \frac{\partial F}{\partial a_2} \right)^2 \quad . \tag{23}$$

Though data in this report have not been so treated, it is a straightforward extension to include a term inside the parentheses of Eq. (22) for the uncertainty (i.e., the variance) of $N_R$ as determined from the Raman scattering experiment. Failure to do that causes a slight underestimation of $\Delta n_e$.

## 6. THOMSON SCATTERING MEASUREMENTS

To this point the laser scattering system has been described both from the hardware point of view and the data manipulation point of view. The versatility of the system has allowed a vast amount of data to be accumulated and analyzed with reasonable assurance

that calculated plasma parameters are indeed correct. The insight into plasma scaling in EBT has been tremendous. In this section, general conclusions of these observations will be listed, along with samples of processed data that led to the conclusions.

As a first example, the radial scanning capability is demonstrated. For a particular power and pressure, Figs. 11 and 12 show the radial dependence of $T_e$ and $n_e$, assuming a Maxwellian distribution. The error bars are plus and minus one standard deviation. Rather than the customary 10 shots per data point, these plots represent over 220 shots. However, the number of shots per point is not equal. An additional detail is that only three wavelength channels were used [$n = 3$ in Eq. (16)]. (There will be comments on this later.) As is seen in Fig. 11, the $T_e$ profile is flat across 20 cm of the core plasma. Many scans of $T_e(r)$ show this same behavior. There exists no reliable evidence to the contrary. A similar conclusion is appropriate for $n_e(r)$, but it is not as strong. The error bar at 8 cm is one indication. As seen in Table 1, the sensitivity of the system is less at the ends of the scan. Consequently, the error in determining that sensitivity is larger. (The $T_e$ measurement is independent of this.) The variations from a flat profile in Fig. 12 are believed to be statistical phenomena rather than real disturbances in $n_e(r)$.

The pressure dependence of the EBT plasma is well documented.[9] The correlation of central laser $n_e$ versus $p_0$ for standard EBT operation with 100 kW of power is shown in Fig. 13 with a shape very much like the interferometer data. Clearly, as $p_0$ is reduced, the plasma changes modes around 10 $\mu$torr, and the density stabilizes. The fluctuation level, as measured by the amplitude of the error bars, is a minimum as $p_0$ is reduced below the transition point. At the lowest pressures, the fluctuations begin to build up again.[10]

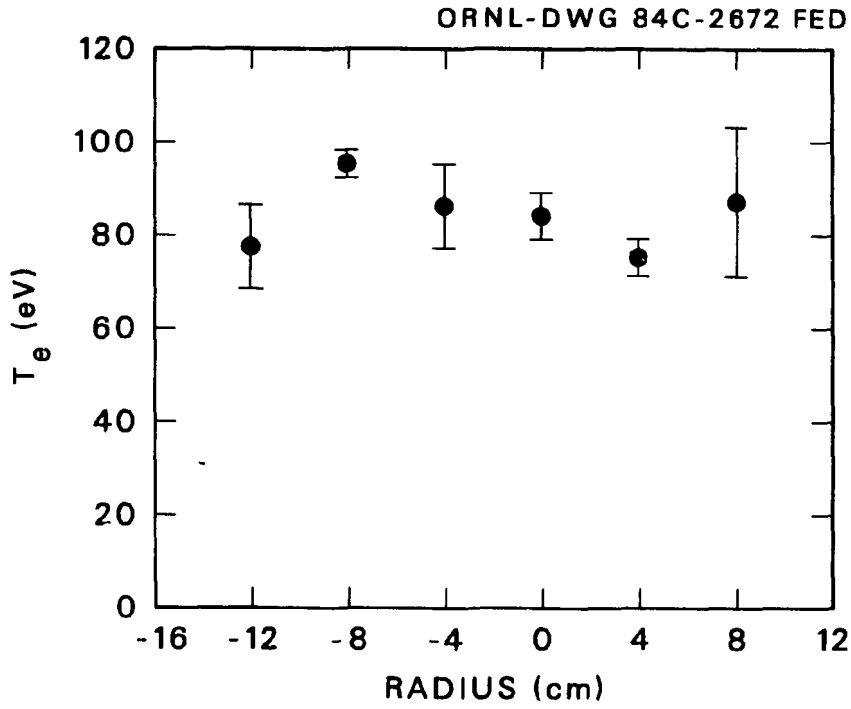


**Fig. 11. The radial dependence of $T_e$ for 150 kW of power at a pressure of 8 μtorr.** The machine center is $r = 0$.

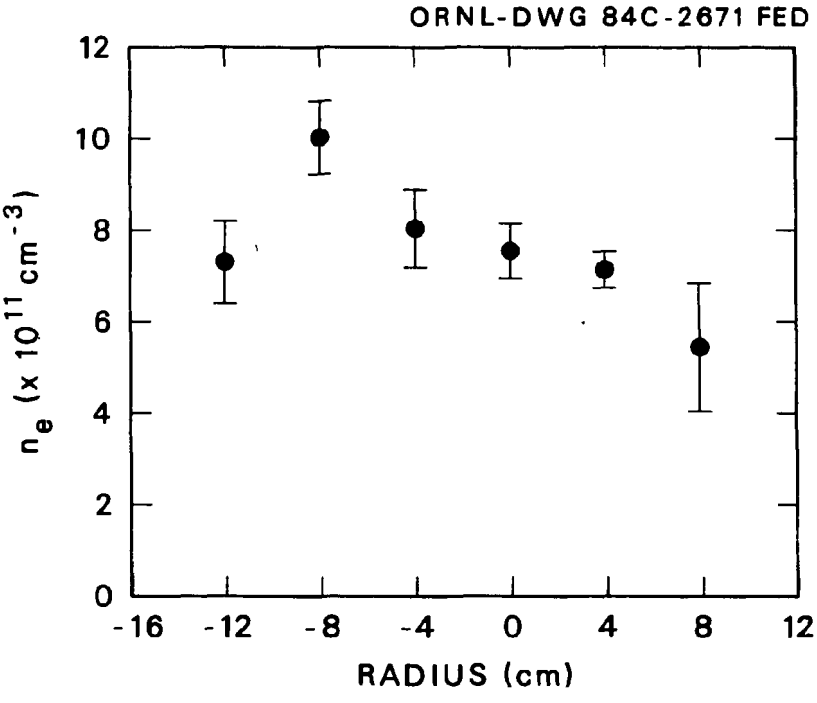


**Fig. 12. The radial dependence of $n_e$ for 150 kW of power at a pressure of 8 μtorr.**

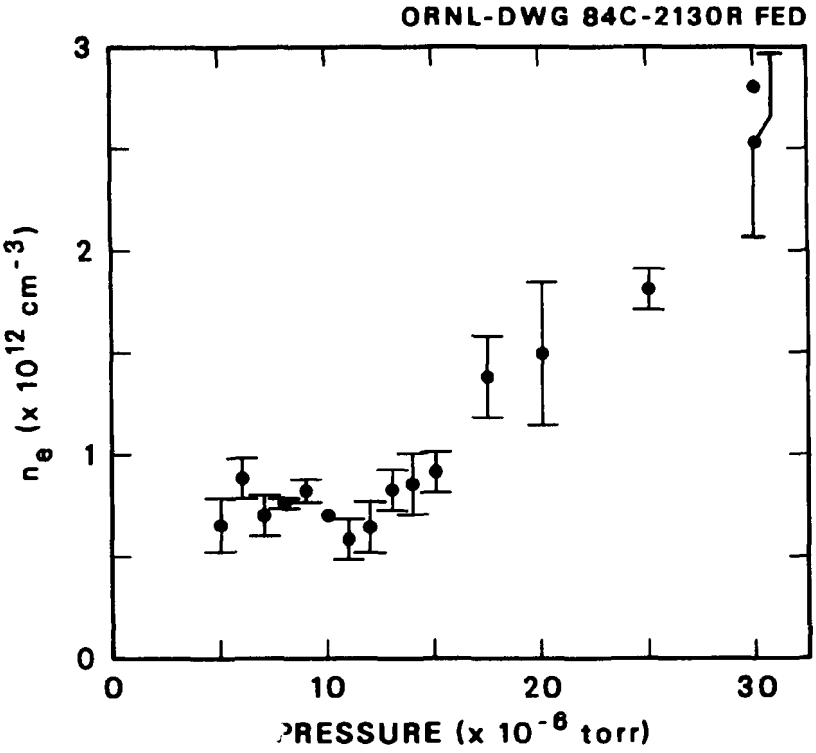


**Fig. 13. The pressure dependence of $n_e$ as measured by the laser.** The microwave power is 100 kW.

As the pressure is reduced with constant microwave power, the power per particle increases, of course, and $T_e$ is expected to increase. Even in the low-pressure regime where core density is constant, the enhanced plasma stability is expected to permit higher temperature. That this is indeed the case is seen in Fig. 14. For the lowest temperatures, the spectra are essentially two-point spectra; there is no signal or only very small signal (less than one photon per shot) in the third data channel.

Other $T_e$ diagnostics[11] show the same variation with pressure, but the values of $T_e$, as measured with soft X rays for example, are a factor of 5 to 10 greater than laser values. The present understanding is that a low-density suprathermal tail builds up as pressure is reduced. This may be modeled by using a bi-Maxwellian distribution. Equation (10) gains

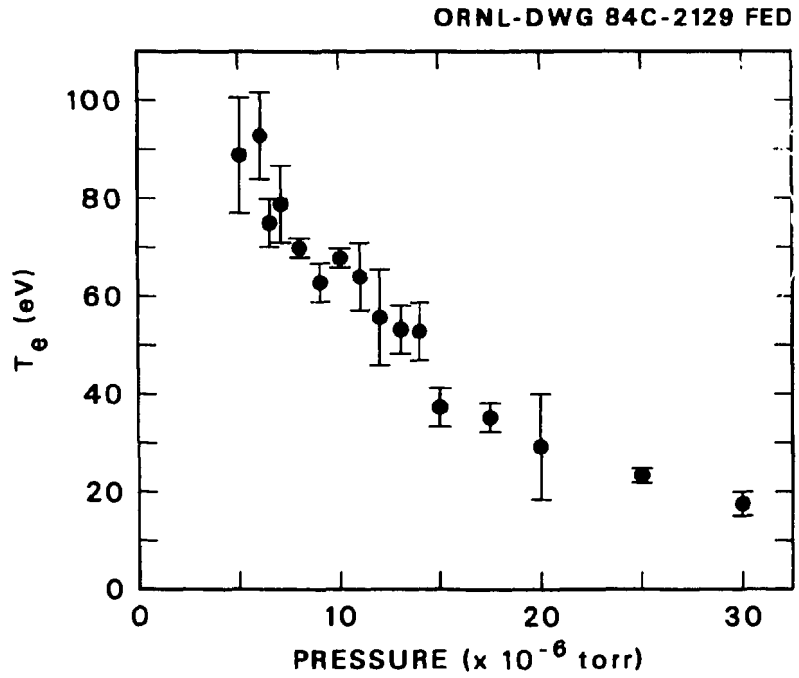


**Fig. 14. $T_e$ as a function of pressure with 100 kW.**

a second term that is identical to the first, except that the second term will refer to a warmer electron component. Two more unknown parameters are introduced, $a_3$ and $a_4$. The first is related to the hot density in the same way as $a_1$ is related to the cold density. Similarly, $a_4$ is related to the hot temperature in an equation like Eq. (11). In practice, $a_4$ is defined as the temperature measured by the soft X-ray diagnostic, so the number of unknowns is reduced to three. All six data channels are used, and the best fit allows calculation of the relative densities of the cold and warm components. Figure 15 shows a spectrum taken for 8 $\mu$torr with 150 kW of microwave power. The X-ray–determined temperature was 490 eV. It is obvious that the spectrum shows something in excess of a Maxwellian. The question becomes, "Can the data be believed?" This issue dramatically focuses on the calibration procedure. By virtue of the comparison of the Raman line

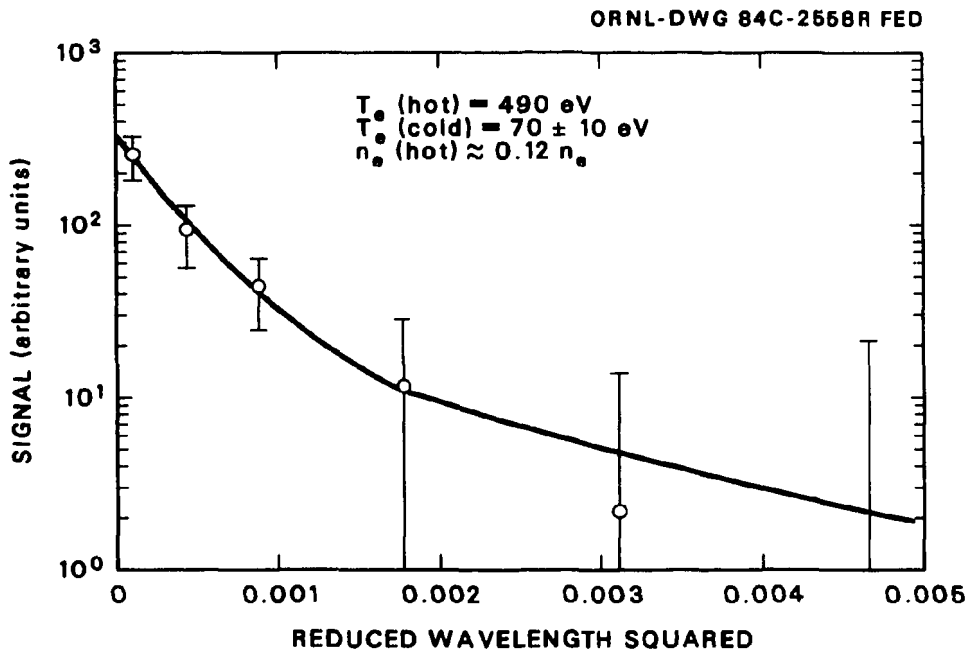


**Fig. 15. A 50-shot laser spectrum fit to a bi-Maxwellian model.** The combined electron density is $1 \times 10^{12}\,cm^{-3}$.

intensities, as described earlier, it is thought that the calibration is accurate and that the expected errors cannot account for the surplus either. In this sequence, 50 shots were added. The error bars in the figure are one sigma as determined from the 50-shot statistics. This allows for a more precise correction for plasma light. The scattered signal in the fourth channel amounts to 75 photons, with about 13 in the fifth. The signal-to-noise ratio of the fourth channel is 0.5, which means that the signal is well above the statistical fluctuation of the noise. In the fifth channel, the photon number is about equal to the square root of the number of plasma light photons, but in many trials, the trend is well established that extra signal exists in the outer channels.

In a separate exercise with the same data, the hot density may be varied in an ad hoc fashion. The weighted sum of the squares of the residuals is shown compared to the percentage of hot particles in Fig. 16. The minimum value corresponds to the values in

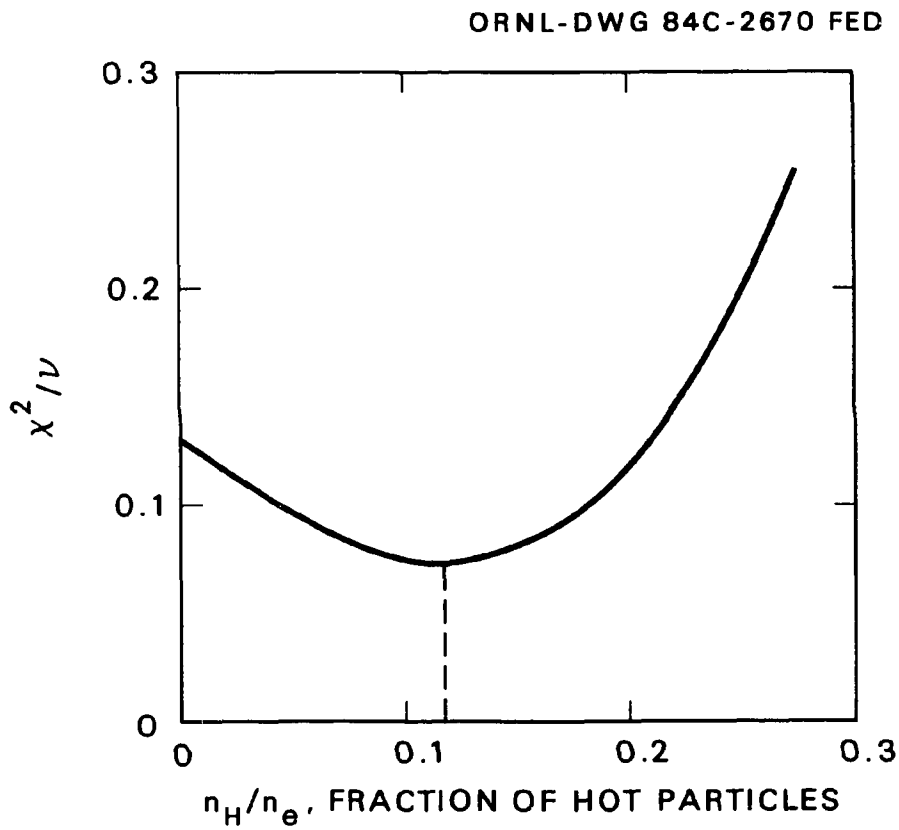


**Fig. 16. Chi-square [equal to $S$ in Eq. (15)] divided by the degrees of freedom vs the fraction of hot electrons.**

Fig. 15, where 12% of the distribution is in the hot tail. Three observations may be made at this point.

1. One sees from Fig. 16 that, on the basis of laser data only, no tail at all is as likely as one involving 20% of the distribution. Nevertheless, a majority of the low-pressure laser sequences indicates the presence of warm electrons in concentrations of 10 to 20%. Additionally, the nonlaser evidence for warm electrons is considerable.

2. By the same token, it is clear that the bulk electron temperature is less than 100 eV, rather than hundreds of electron volts. Later X-ray measurements were found to be consistent with this view.
3. The normalized values of chi-square $S/\nu$ are considerably less than unity [see Eq. (16)]. This does not indicate that the fit is good, only that the variance of the data is large. The variance is, in fact, about twice what is expected based on Poisson statistics. This is due, in some part, to the variation of plasma light, plasma fluctuations, and the pulse-height distribution of the photomultiplier tubes.

The conclusion from these considerations is that, in this case, on the order of 10% of the electron population is in a suprathermal distribution. The density of the component is about $10^{11}$ cm$^{-3}$. Unfortunately, the quality of the laser searches for these components, say during a pressure scan or as a function of radius, is poor. The time to take a 50-shot spectrum is such that the data are limited to 10-shot sequences for which the confidence is much lower. In any event, these observations provide for a reconciliation of $T_e$ diagnostics and illustrate the need to allow for power flow between components in power balance calculations.[12]

The scaling of electron parameters with magnetic field merits discussion.[13] This topic also provides a good example of the strengths and weaknesses of the Thomson scattering system. A series of 10-shot sequences was collected for seven different field currents from 5400 to 7250 A at two radial positions in the plasma. The idea was to look for any indication of the second harmonic of the electron cyclotron resonance zone passing the outer

position as the field changed. Regarding the suprathermal component, no definite conclusion could be reached. What could have been a tail was observed in 11 of the 14 spectra, but the pattern was irregular. With a simple Maxwellian model, it seems possible for the selected pressure (9.8 $\mu$torr) and power (150 kW) that density depends linearly on magnetic field at both radii (see Fig. 17). The temperature on-axis ($r = 0$) is constant or increases slightly at lower fields. At 8 cm outboard, $T_e$ appears to decrease as the field is lowered (see Fig. 18). The resonance position is at 8 cm with a current of 6400 A. At 7250 A (the standard case), the measurements are consistent with the flat temperature

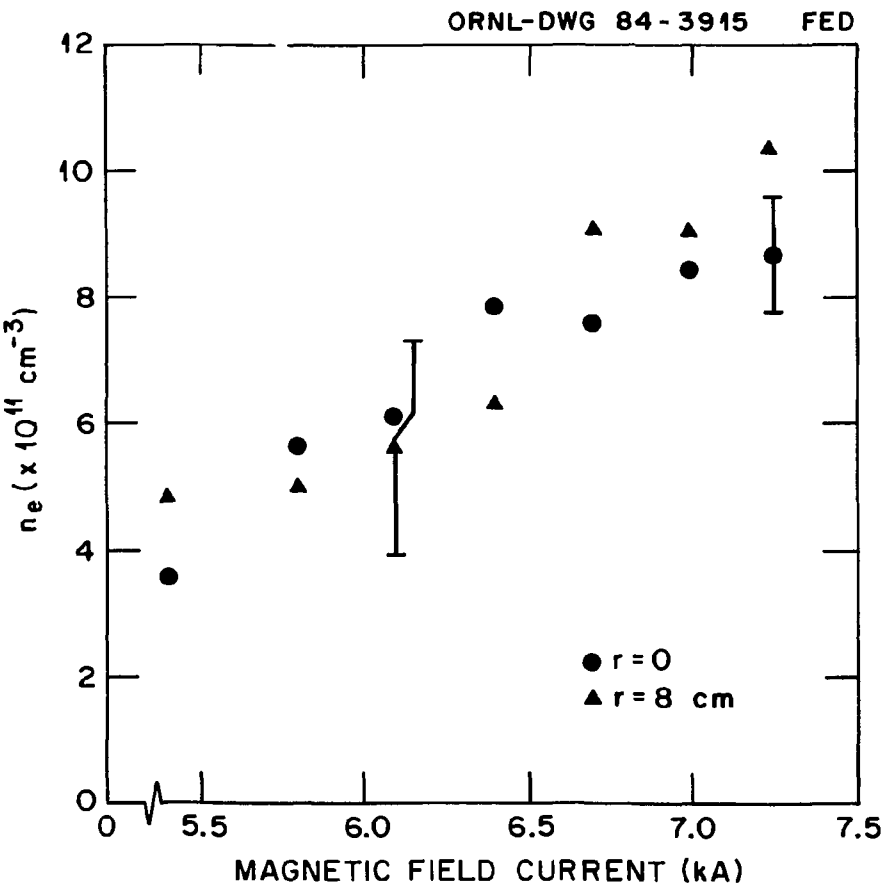


**Fig. 17. The dependence of $n_e$ on magnetic field as determined with four-point Maxwellian fits.** Power and pressure are 150 kW and 9.8 $\mu$torr respectively.

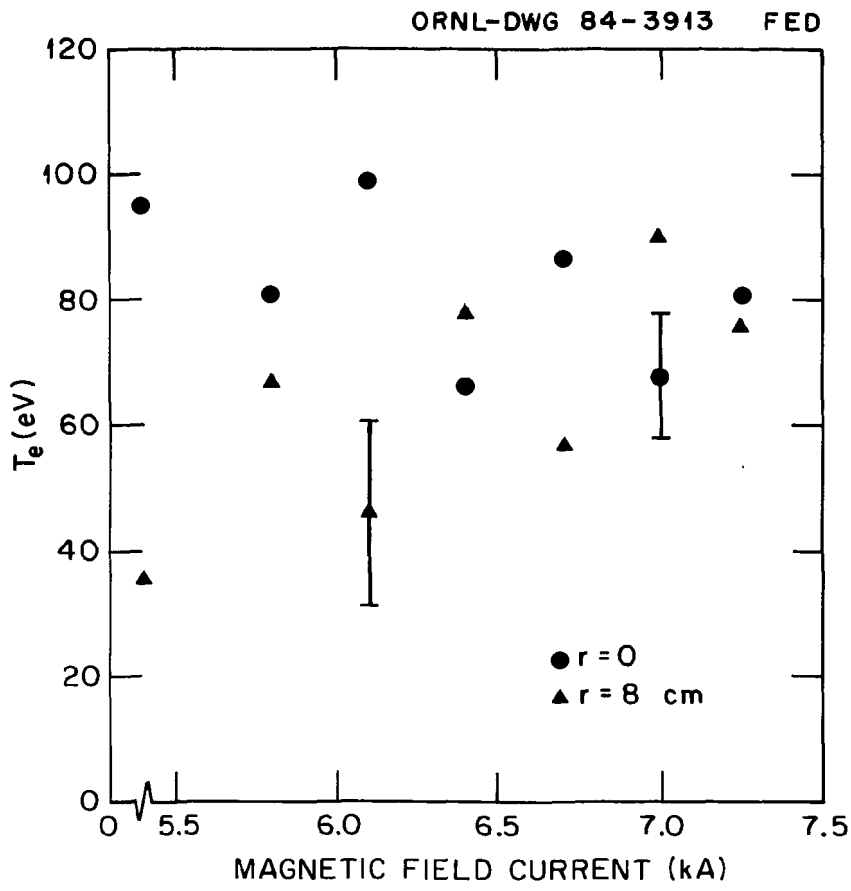


**Fig. 18. The dependence of $T_e$ on magnetic field as determined with four-point Maxwellian fits for the same conditions as Fig. 17.**

profile of Fig. 11; therefore, local plasma pressure is seen to fall faster at 8 cm than on-axis, as the field is reduced.

A final example of system capability is the results of an experiment with microwave modulation.[14] In this endeavor, pressure was held constant at 8 μtorr. Microwave power was pulsed from 90 kW every quarter second to 150 kW for about 50 ms. Figure 19 shows the decay of $T_e$ in the plasma core as the microwave power falls from the higher level. Because the $n_e$ modulation is comparable with the error bar, the energy confinement time is approximately the same as the relaxation time of $T_e$ if the microwave power fall time is

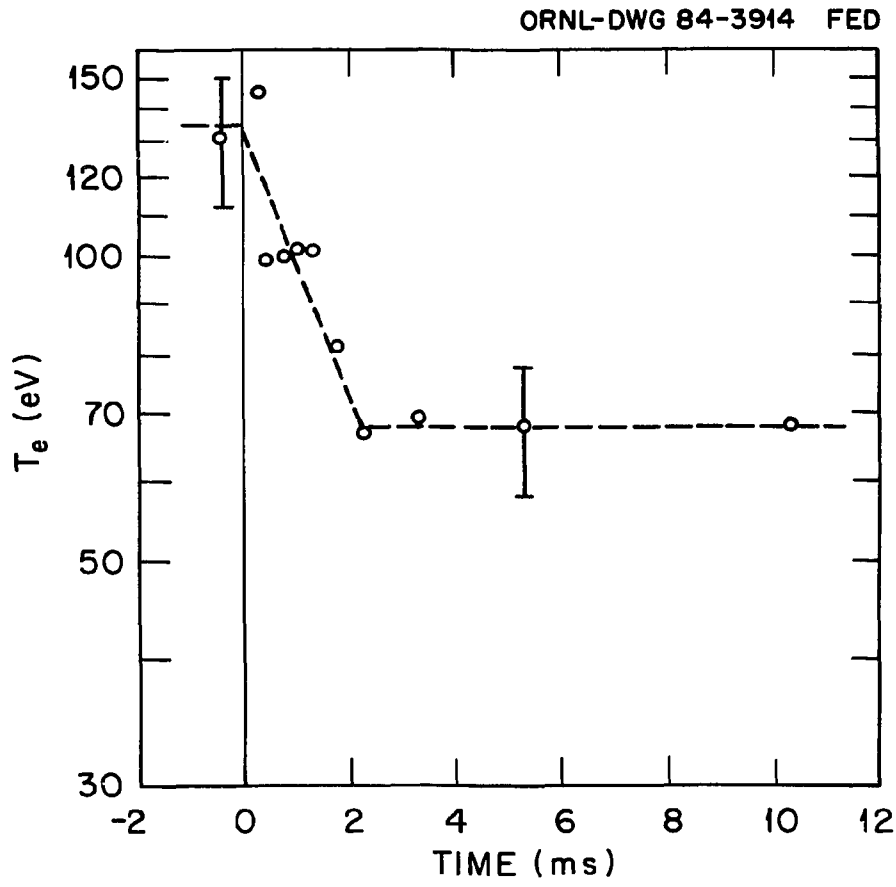


**Fig. 19. The evolution of $T_e$ during a pulsed microwave turn-down experiment.** The pressure is fixed at 8 $\mu$torr.

short enough. In any case, the measured time represents the maximum local energy confinement time—about 0.5 ms for these conditions. Each data point is generated by a 10-shot sequence with external triggering of the laser. The time difference is selected with a digital delay generator and is checked against the delay between the interferometer signal and a Pockels cell sync pulse. The resulting decay time is the same order of magnitude as one calculates by assuming a 300-L plasma that absorbs about a fourth of the available power in the core. One novelty of this exercise is that the peak $T_e$ exceeds the steady-state,

150-kW plasma temperature by 50%. This is perhaps due to the absence of the usual high-energy rings,[15] which are not established in the 50 ms during which the power is high. The 90-kW parameters, on the other hand, are the same as the steady-state values.

# 7. CONCLUSIONS

This report has outlined a successful approach to a formidable plasma measurement. Nowhere else in the world, with the possible exception of the Nagoya Bumpy Torus,[16] has Thomson scattering on a thermal laboratory plasma been accomplished at such low density. The key elements have been the giant ruby laser and the details of the optical system described herein. The result has been a system, hardened against the plasma environment, that is able to survive for long periods of time and obtain useful data with $n_e$ as low as $2 \times 10^{11}$ cm$^{-3}$. Perhaps the greatest contribution to EBT physics has been the demonstration that the bulk electron temperature is below 100 eV. Nevertheless, bolstered by redundant calibration procedures, the Thomson spectra enable observation of a $10^{11}$-cm$^{-3}$ suprathermal component, thus reconciling a long-standing discrepancy among $T_e$ diagnostics.

The final purpose of these notes is to assist in the planning of future laser scattering diagnostics that deal with low-density, steady-state plasma with adverse conditions for system survival. There are several recommendations for improving on the present experiment. The first is to increase the number of data channels so that signal is ordinarily present even in the absence of a tail in perhaps six instead of three channels. For EBT conditions, the polychromator could be modified in either of two ways:

1. A grating with higher dispersion could be used, which would spread the signal across more of the existing channels.
2. Alternatively, narrower fiber optic bundles could be used with the same results. (An assortment of smaller bundles was actually purchased but never installed.)

Either way, the signal levels would be somewhat lower, but the signal-to-noise ratio should not suffer. A second recommendation is to abandon the gated integrators in favor of waveform digitizers. One 200-MHz device* for each channel would be required. Advantages are that no division of the signals by 2 is required, the problems of calibration of pairs of integrators disappear, and a better record of plasma light is obtained. In fact, the whole calibration effort is simplified. Relative quantum efficiency becomes very easy to measure, as well as response per event. Disadvantages are the large capital cost and the proliferation of data to thousands of records per shot. A last consideration is whether to change laser wavelength. A Nd:YAG laser was once considered. Frequency doubled to 532 nm, the laser light would be in a wavelength range in which the quantum efficiency and durability of phototubes is superior to gallium arsenide tubes and in which the inherent plasma light is reduced. Over 20 J of green light is available essentially by simply changing the laser heads on the existing system. At one time this option was not selected because of a lack of confidence in the performance of the doubling crystal. Other disadvantages include the presence of tens of joules of the fundamental wavelength, which is not frequency doubled, and, of course, the cost.

*A Tektronix 7612D, for example.

# REFERENCES


1. J. C. Glowienka, "ELMO Bumpy Torus: An Alternate Concept to Tokamaks and Mirrors," *J. Vac. Sci. Technol.* **18**(3), 1088 (1981); L. A. Berry et al., "Recent Advances in Confinement and Heating Physics on EBT-S," presented at the 10th International Conference on Plasma Physics and Controlled Nuclear Fusion Research, London, Sept. 12–19, 1984.
2. R. A. Dandl et al., "Plasma Confinement and Heating in the ELMO Bumpy Torus (EBT)," in *Plasma Physics and Controlled Nuclear Fusion Research, 1974* (IAEA, Vienna, 1975), vol. 2, p. 141; R. A. Dandl et al., *Summary of EBT-I Experimental Results*, ORNL/TM-6457, Oak Ridge Natl. Lab., October 1978.
3. E. Fünfer, B. Kronast, and H. J. Kunze, "Experimental Results on Light Scattering by a $\theta$-Pinch Plasma Using a Ruby Laser," *Phys. Lett.* **5**(2), 125 (1963); N. J. Peacock et al., "Measurement of the Electron Temperature by Thomson Scattering in Tokamak T3," *Nature* **224**, 488 (1969); N. Bretz et al., "Multi-channel Thomson Scattering Apparatus," *Appl. Opt.* **17**(2), 192 (1978).
4. D. H. McNeill and R. A. Dandl, "Thomson Scattering Determination of Electron Temperature in ELMO Bumpy Torus (EBT)," presented at the Topical Conference on Diagnostics of High Temperature Plasmas, Knoxville, Tennessee, 1976.
5. J. A. Cobble, R. A. Dandl, and M. Hesse, "Thomson Scattering on EBT-S," *Bull. Am. Phys. Soc.* **23**(7), 877 (1978); L. Bighel and J. A. Cobble, "Electron Heating and Confinement Measurements in the EBT-S Toroidal Core Plasma with Thomson

Scattering," *Phys. Rev. Lett.* **46**(6), 430 (1981); J. A. Cobble and L. Bighel, "Thomson Scattering Diagnostic for a Low-Density, High-Temperature, Steady-State Plasma," *Rev. Sci. Instrum.* **53**(4), 436 (1982); J. A. Cobble, "Thomson Scattering at Plasma Densities Below $10^{12}$ $cm^{-3}$," *Rev. Sci. Instrum.* **56**(1), 73 (1985); J. A. Cobble, "The Evolution of Low-Density Thomson Scattering on EBT," presented at the 5th Topical Conference on Diagnostics of High Temperature Plasma, Tahoe City, California, 1984, to be published in *Rev. Sci. Instrum.*

6. D. H. McNeill, "Ruby Filter for Stray Light Reduction in Scattering Experiments," *Appl. Opt.* **15**, 573 (1976).
7. H. Röhr, "Rotational Raman Scattering of Hydrogen and Deuterium for Calibrating Thomson Scattering Devices," *Phys. Lett.* **81A**(8), 451 (1981).
8. J. R. Wolberg, Chap. 3 in *Prediction Analysis*, D. Van Nostrand, Princeton, New Jersey, 1967.
9. R. J. Colchin et al., "Plasma Properties in the ELMO Bumpy Torus," *Plasma Phys.* **25**(6), 597 (1983).
10. A. Komori, *Observations of Low-Frequency Plasma Fluctuations in ELMO Bumpy Torus*, ORNL/TM-7906, Oak Ridge Natl. Lab., October 1984.
11. D. L. Hillis, G. R. Haste, and L. A. Berry, "Electron Confinement Studies on the EBT-S Bumpy Torus Experiment using Soft X-ray Techniques," *Phys. Fluids* **26**(3), 820 (1983); R. K. Richards, "Analysis of EBT Plasmas and Confinement Including Electron Temperature Measurements from Inner Shell Ionization," presented at the 4th Topical Conference on Atomic Processes in High Temperature Plasmas, Princeton, New Jersey, 1983.

12. D. W. Swain, J. A. Cobble, D. L. Hillis, R. K. Richards, and T. Uckan, "The Electron Distribution Function in ELMO Bumpy Torus," submitted to *Phys. Fluids.*

13. J. C. Glowienka and J. A. Cobble, "Observed Variation of Plasma Parameters with Magnetic Field in EBT," *Bull. Am. Phys. Soc.* **27**(8), 1114 (1982).

14. F. M. Bieniosek et al., "Pulsed Experiments on EBT-S," *Bull. Am. Phys. Soc.* **29**, 1417 (1984).

15. N. A. Uckan, ed., *Proceedings of the Second Workshop on Hot Electron Ring Physics*, CONF-811203, Oak Ridge Natl. Lab., 1981.

16. R. J. Colchin and J. C. Glowienka, *Comparison of Plasma Results in EBT-I and NBT-1M*, ORNL/TM-9128, Oak Ridge Natl. Lab., July 1984.

ORNL/TM-9471
Dist. Category UC-20 f,g

*INTERNAL DISTRIBUTION*

1. F. W. Baity
2–6. J. A. Cobble
7. W. A. Davis
8. R. A. Dory
9. G. R. Haste
10. D. L. Hillis
11. S. Hiroe
12. J. K. Johnson
13. H. D. Kimrey
14. P. W. King
15. L. W. Owen
16. T. L. Owens
17. M. J. Saltmarsh
18. J. Sheffield
19. D. A. Spong
20. D. W. Swain
21. T. Uckan
22. J. B. Wilgen
23–24. Laboratory Records Department
25. Laboratory Records, ORNL-RC
26. Document Reference Section
27. Central Research Library
28. Fusion Energy Division Library
29. Fusion Energy Division Publications Office
30. ORNL Patent Office

*EXTERNAL DISTRIBUTION*

31. W. B. Ard, McDonnell Douglas Astronautics Company, Bldg. 278, P.O. Box 516, St. Louis, MO 63166
32. J. Barter, Lawrence Livermore National Laboratory, University of California, P.O. Box 808, Livermore, CA 94550
33. H. L. Berk, Institute of Fusion Studies, University of Texas at Austin, Robert L. Moore Hall, Rm. 11.218, Austin, TX 78712
34. Bibliotheque, Centre de Recherches en Physique des Plasmas, 21 Avenue des Bains, 1007 Lausanne, Switerzerland
35. Bibliothek, Institut fur Plasmaphysik, D-8046 Garching bei Munchen, Federal Republic of Germany
36. Bibliothek, Institut fur Plasmaphysik, KFA, Postfach 1913, D-5170, Federal Republic of Germany
37. Bibliotheque, Service du Confinement des Plasmas, CEA, B.P. No. 6, 92 Fontenay-aux-Roses (Seine), France
38. F. M. Bieniosek, McDonnell Douglas Astronautics Company, Bldg. 278, P.O. Box 516, St. Louis, MO 63166
39. J. D. Callen, Department of Nuclear Engineering, University of Wisconsin, Madison, WI 53706
40. R. W. Conn, Department of Chemical, Nuclear and Thermal Engineering, University of California, Los Angeles, CA 90024
41. R. A. Dandl, Applied Microwave Plasma Concepts, 2210 Encinitas Blvd., Suite P, Encinitas, CA 92024

42. N. A. Davies, U.S. Department of Energy, Office of Fusion Energy, Office of Energy Research, Mail Station G-256, Washington, DC 20545
43. S. O. Dean, Director, Fusion Energy Development, Science Applications, Inc., 2 Professional Drive, Suite 249, Gaithersburg, MD 20760
44. Documentation S.I.G.N., Department de la Physique du Plasma et de la Fusion Controllee, Centre d'Etudes Nucleaires, B.P. 85 Centre de Tri, 38041 Cedex, Grenoble, France
45. G. A. Eliseev, I. V. Kurchatov Institute of Atomic Energy, P.O. Box 3402, 123182 Moscow, U.S.S.R.
46. A. J. Favale, Grumman Aerospace Corporation, South Oyster Bay Road, P.O. Box 31, Bethpage, NY 11714
47. H. K. Forsen, Bechtel Group, Inc., Research Engineering, P.O. Box 3965, San Francisco, CA 94105
48. M. Fujiwara, Institute of Plasma Physics, Nagoya University, Nagoya 464, Japan
49. T. V. George, Office of Fusion Energy, Office of Energy Research, Mail Station G-256, Department of Energy, Washington, DC 20545
50. G. G. Gibson, Westinghouse Electric Corp., Fusion Power Systems, Dept. C, P.O. Box 10864, Pittsburgh, PA 15236
51. V. A. Glukhikh, Scientific-Research Institute of Electro-Physical Apparatus, 188631 Leningrad, U.S.S.R.
52. R. W. Gould, Department of Applied Physics, California Institute of Technology, Pasadena, CA 92024
53. R. L. Hickok, Rensselaer Polytechnic Institute, ESE Department, Engineering Building, Troy, NY 12181
54. H. Ikegami, Institute of Plasma Physics, Nagoya Univ., Nagoya 464, Japan
55. H. R. Jory, Varian Associates, 611 Hansen Way, Palo Alto, CA 94303
56. A. Komori, Interdisplinary Graduate School of Engineering Sciences, Kyushu University, Kasuga, Fukuoka 816, Japan
57. N. A. Krall, Jaycor, 11011 Torreyana Rd., P.O. Box 85154, San Diego, CA 92138
58. K. Krause, Lawrence Livermore National Laboratory, P.O. Box 808, Livermore, CA 94550
59. J. Lassoon, TRW Defense and Space Systems, 1 Space Park, Bldg. R-1, Redondo Beach, CA 92078
60. N. H. Lazar, TRW Defense and Space Systems, 1 Space Park, Bldg. R-1, Redondo Beach, CA 92078
61. Library, Culham Laboratory, UKAEA, Abingdon, Oxfordshire, OX14 3DB, England
62. Library, FOM Instituut voor Plasma-Fysica, Rijnhuizen, Jutphaas, Netherlands
63. Library, Institute of Physics, Academia Sinica, Peking, Peoples Republic of China
64. Library, Institute for Plasma Physics, Nagoya University, Nagoya 464, Japan
65. Library, International Centre for Theoretical Physics, Trieste, Italy
66. Library, Laboratoria Gas Ionizzati, Frascati, Italy
67. Library, Plasma Physics Laboratory, Kyoto University, Gokasho, Uji, Kyoto, Japan
68. D. G. McAlees, Exxon Nuclear Company, Inc., 777 106th Avenue, NE, Richland, WA 98009
69. J. B. McBride, Science Applications, Inc., 1200 Prospect Street, P.O. Box 2351, La Jolla, CA 92037

70. D. H. McNeill, Plasma Physics Lab., Princeton University, P.O. Box 451, Princeton, NJ 08544
71. K. Mizuno, University of California-Davis, Applied Science Dept., 228 Walker Hall, Davis, CA 95617
72. Plasma Research Laboratory, Australian National University, P.O. Box 4, Canberra ACT, 2000, Australia
73. B. H. Quon, JAYCOR, San Diego, CA 92138
74. P. J. Reardon, Princeton Plasma Physics Laboratory, P.O. Box 451, Princeton, NJ 08544
75. F. L. Ribe, College of Engineering, AERL Building, FL-10, University of Washington, Seattle, WA 98195
76. D. D. Ryutov, Institute of Nuclear Physics, Siberian Branch of the Academy of Sciences of the U.S.S.R., Sovetskaya St. 5, 630090 Novosibirsk, U.S.S.R.
77. T. K. Samec, TRW Defense and Space Systems, 1 Space Park, Bldg. R-1, Redondo Beach, CA 92078
78. I. Shpigel, Lebedev Physical Institute, Leninsky Prospect 53, 117924 Moscow, U.S.S.R.
79. B. W. Stallard, Lawrence Livermore National Laboratory, P.O. Box 808, Livermore, CA 94550
80. Thermonuclear Library, Japan Atomic Energy Research Institute, Naka, Ibaraki, Japan
81. V. T. Tolok, Kharkov Physical-Technical Institute, Academical St. 1, 310108, Kharkov, U.S.S.R.
82. J. M. Turner, Office of Fusion Energy, Office of Energy Research, Mail Station G-256, Department of Energy, Washington, DC 20545
83. R. Varma, Physical Research Laboratory, Navrangpura, Ahmedabad, India
84. H. Weitzner, New York University, Courant Institute of Mathematical Sciences, 251 Mercer Street, New York, NY 10012
85. Office of the Assistant Manager for Energy Research and Development, Department of Energy, Oak Ridge Operations, P.O. Box E, Oak Ridge, TN 37830

86–293. Given distribution as shown in TID-4500, Magnetic Fusion Energy (Distribution Category UC-20 f,g: Theoretical Plasma Physics and Experimental Plasma Physics)